

Constraints on circum-galactic media from Sunyaev-Zel'dovich effects and X-ray data

XUANYI WU,¹ HOUJUN MO,² CHENG LI,¹ AND SEUNGHWAN LIM³

¹*Department of Astronomy, Tsinghua University, Beijing 100084, China*

²*Department of Astronomy, University of Massachusetts, Amherst, MA01003, USA*

³*Department of Physics and Astronomy, University of British Columbia, 6224 Agricultural Road, Vancouver, BC V6T 1Z1, Canada*

Submitted to ApJ

ABSTRACT

We use observational measurements of thermal and kinetic Sunyaev-Zel'dovich effects, as well as soft X-ray emission associated with galaxy groups to constrain the gas density and temperature in the circumgalactic medium (CGM) for dark matter halos with masses above $10^{12.5}M_{\odot}$. A number of generic models are used together with a Bayesian scheme to make model inferences. We find that gas with a single temperature component cannot provide a consistent model to match the observational data. A simple two-phase model assuming a hot component and an ionized warm component can accommodate all the three observations. The total amount of the gas in individual halos is inferred to be comparable to the universal baryon fraction corresponding to the halo mass. The inferred temperature of the hot component is comparable to the halo virial temperature. The fraction of the hot component increases from (15 – 40)% for $10^{12.5}M_{\odot}$ halos to (40 – 60)% for $10^{14.5}M_{\odot}$ halos, where the ranges reflect uncertainties in the assumed gas density profile. Our results suggest that a significant fraction of the halo gas is in a non-thermalized component with temperature much lower than the virial temperature.

Keywords: methods: statistical – galaxies: formation – galaxies: evolution – galaxies: halos

1. INTRODUCTION

In the current paradigm of structure formation, galaxies are assumed to form and evolve in dark matter halos (see Mo et al. 2010, for a review). In this scenario, accretion and feedback together govern the growth of galaxies. The circum-galactic medium (hereafter CGM) is the repository for baryons, through which galaxies are connected to the intergalactic medium (IGM). Some of these baryons will be accreted by galaxies to form stars and central super-massive black holes, while most of them leave galaxies through outflows produced by supernova and quasars. Much of the ejected gas may be re-accreted, and so the gas may cycle through the CGM a number of times. Currently, the evidence for this paradigm is indirect, mainly from investigations of galaxy stellar masses, metallicities, and star-formation rates over cosmic time. To study this paradigm directly,

however, one needs to focus on the CGM, the ground zero for gas accretion and ejection.

The properties of the CGM has been studied in a number of ways. X-ray observations have been conducted to study the intra-cluster medium (ICM) in galaxy clusters and groups (e.g. Wang et al. 2014; Anderson et al. 2015). The results demonstrate that substantial amounts of gas heating is actually by non-gravitational sources, likely from the feedback of member galaxies (Cavaliere et al. 1998; Arnaud & Evrard 1999; Helsdon & Ponman 2000; Kravtsov & Yepes 2000; Babul et al. 2002; McCarthy et al. 2011). A complementary way to study the CGM is through the Sunyaev-Zel'dovich effect (hereafter SZE; Sunyaev & Zeldovich 1972) of free electrons on the spectrum of the cosmic microwave background (CMB) owing to inverse Compton scattering. The thermal SZE (hereafter tSZE) is proportional to the line-of-sight integral of the electron pressure (or thermal energy density), while the kinetic SZE (kSZE) is proportional to the integral of the momentum density along a given line of sight, thus providing two independent constraints on

the properties of the ionized part of the CGM. Great efforts have been made to measure the SZE using CMB surveys, such as *Planck*¹, the Atacama Cosmology Telescope (*ACT*)², and the South Pole Telescope (*SPT*)³. For example, using a sample of galaxy groups covering a large range of halo masses together with the *Planck* Compton parameter map (Planck Collaboration et al. 2014), Lim et al. (2018) found that the thermal content of the gas in low-mass halos is significantly lower than that expected from the simple self-similar model, where the halo gas is assumed to be at the virial temperature and to have a mass given by the universal baryon fraction. By stacking galaxy groups with known masses and peculiar velocities in *Planck* maps, Lim et al. (2020) found that the total kSZE within halos implies a baryon to dark matter mass ratio that is comparable to the universal baryon fraction. The tSZE and kSZE results combined, therefore, indicate that not all the halo gas is at the virial temperature (Lim et al. 2020).

Clearly, these observational results provide important information about the properties of the CGM. In this paper, we use the combination of SZE observations and soft X-ray data to constrain the density and temperature of the CGM. We use a set of generic models to show what we can learn from the observational data. The paper is organized as follows. We describe the observational data used in our analysis in §2, and models of halo gas in §3. Our analysis and results are presented in §4. Finally, we summarize and discuss our results in §5. Throughout the paper, we adopt a flat universe with matter density $\Omega_m = 0.308$ and the reduced Hubble constant $h = 0.678$, as given in Planck Collaboration et al. (2016a).

2. OBSERVATIONAL DATA

2.1. Thermal SZE

The thermal Sunyaev-Zel'dovich effect (tSZE) is produced by the inverse Compton scattering of CMB photons as they encounter high energy thermal electrons in hot gas (Sunyaev & Zeldovich 1972; Rephaeli et al. 2005). The tSZE presents itself as a distortion in the CMB spectrum, and its strength is characterized by the Compton y -parameter:

$$y \equiv \frac{\sigma_T}{m_e c^2} \int P_e dl, \quad (1)$$

where σ_T is the Thompson cross-section, m_e is the electron mass, $P_e = k_B n_e T_e$ is the electron pressure with

k_B being the Boltzmann constant, n_e the electron number density and T_e the electron temperature. The integration is along the line of sight (LOS). For galaxy groups/halos concerned here, the total tSZE flux within a radius R of an object is described by a quantity Y_R , defined as

$$Y_R = \frac{\sigma_T}{m_e c^2} \frac{1}{d_A^2} \int_{V_R} P_e dV, \quad (2)$$

where d_A is the angular diameter distance of the object, and V_R is the volume within R . The intrinsic tSZE flux can then be expressed in terms of a normalized quantity,

$$\tilde{Y}_R \equiv E^{-2/3}(z) Y_R \left(\frac{d_A(z)}{500 \text{Mpc}} \right)^2, \quad (3)$$

where

$$E(z) = \frac{H(z)}{H_0} = \sqrt{\Omega_m (1+z)^3 + \Omega_\Lambda} \quad (4)$$

is included to make \tilde{Y}_R independent of the redshift for a given halo mass. The intrinsic tSZE, therefore, provides a measure of the thermal energy of electrons.

In our analysis, we use the results obtained by Lim et al. (2018), who used a spatial filter to extract tSZE signals associated with galaxy groups of various halo masses from the Planck NILC all sky tSZ Compton parameter map (Remazeilles et al. 2011; Planck Collaboration et al. 2016b). Lim et al. (2018) assumed that the spatial pressure profile follows the universal pressure profile (UPP) model of Arnaud et al. (2010). They divided galaxy groups into a number of sub-samples according to halo mass and obtained the average tSZE amplitude, \tilde{Y}_{200} , for galaxy groups contained in the same halo mass bin. The quantity \tilde{Y}_{200} is the same as $\tilde{Y}_{R_{200}}$, where R_{200} is the radius within which the mean density of the halo is 200 times the critical density of the universe. We define the halo mass M_{200} as the mass of a halo within R_{200} . Since the Planck observation does not resolve the flux distribution for all individual halos, the values of \tilde{Y}_{200} they obtained should be used in combination with the adopted UPP to get the total tSZE flux of the halo. For our analysis, we convert the observational quantity to

$$P_{200} \equiv \int_{V_{200}} P_e dV. \quad (5)$$

The black data points in the first panel of Figure 1 show P_{200} as a function of M_{200} , while the shadow region represents the error of the measurement. Here M_{200} is the halo mass defined by the dark matter mass enclosed by R_{200} .

2.2. Kinetic SZE

¹ https://www.nasa.gov/mission_pages/planck

² <https://act.princeton.edu>

³ <https://pole.uchicago.edu>

The kSZE is produced by Doppler's effect of CMB photons as they are scattered by electrons associated with galaxy systems that have bulk motion (Sunyaev & Zeldovich 1970):

$$k \equiv \left(\frac{\Delta T}{T_{\text{CMB}}} \right)_{\text{kSZ}} = -\frac{\sigma_T}{c} \int n_e(\mathbf{v} \cdot \hat{\mathbf{r}}) dl, \quad (6)$$

where \mathbf{v} represents the bulk motion peculiar velocity of the gas, $\hat{\mathbf{r}}$ is the unit vector along the LOS in question, and the integration is along the LOS. For halos with known peculiar velocities, one can estimate the following quantity from the kSZE signal:

$$K_{200} \equiv \frac{1}{d_A(z)^2} \sigma_T \int_{V_{200}} n_e dV. \quad (7)$$

From this, one can obtain the intrinsic kSZE flux,

$$\tilde{K}_{200} \equiv K_{200} \left(\frac{d_A(z)}{500 \text{Mpc}} \right)^2. \quad (8)$$

We use the data of \tilde{K}_{200} obtained by Lim et al. (2020) for our analysis. They applied spatial filters to the Planck 100, 143, and 217GHz channel maps to extract kSZE signals of galaxy groups of different masses simultaneously, assuming that n_e follows the profile described in Plagge et al. (2010).

The amplitude of the profile for each group is assumed to depend on its halo mass. Together with the peculiar velocities of individual groups given by Wang et al. (2012), Lim et al. (2020) obtained the amplitude of the ionized gas profile as a function of halo mass by matching the model maps with the observational ones. We use their result of \tilde{K}_{200} as a function of halo mass, M_{200} , which is shown as the black data points in the second panel of Figure 1. The shadow region is the error of the measurement.

2.3. X-ray luminosity

X-ray emissions from galaxy groups/clusters are produced by the hot intra-cluster/group gas generated by bremsstrahlung. The X-ray luminosity depends on the temperature, density and metallicity of the gas and can be written as:

$$L(\nu_1, \nu_2) = \int_V \int_{\nu_1}^{\nu_2} n_e(\mathbf{r}) n_H(\mathbf{r}) \epsilon_X(T, \nu, Z) dV d\nu, \quad (9)$$

where ν_1 and ν_2 specify the frequency range, n_H is the total hydrogen number density, and $\epsilon_X(T, \nu, Z)$ is the emissivity at the temperature T , frequency ν and metallicity Z . We use the Astrophysical Plasma Emission Code (APEC) to calculate the emissivity. The code includes physical processes such as bremsstrahlung, radiative recombination and two-photon radiation. The exact

assumption of the metallicity does not have a significant impact on our results and we use $Z = 0.05Z_\odot$ here. For our analysis, we use the X-ray measurements from Anderson et al. (2015), who obtained the X-ray luminosity for halos of different masses by using the ROSAT All-Sky Survey (RASS). They extracted an average X-ray luminosity for locally brightest galaxies (LBGs) of a given stellar mass by stacking the X-ray images around them, using the LBG sample of Planck Collaboration et al. (2013). They used numerical simulation to validate their method. For high-mass galaxies, they converted the galaxy stellar mass into a halo mass using the simulation calibrations presented in Planck Collaboration et al. (2013). For low-mass systems, they used an abundance matching method to estimate M_{500} from the stellar mass. Their final results are summarized as the X-ray luminosity, $L_{X,500}$, in the energy range between 0.5 and 2 KeV within the radius of R_{500} . Here R_{500} is the halo radius within which the mean density is 500 times the critical density of the universe, and M_{500} is the dark matter mass enclosed by R_{500} . Their results for the $L_{X,500}$ - M_{200} relation are shown as the black data points in the third panel of Figure 1. Here we convert M_{500} into M_{200} assuming a NFW profile. We note that the $L_{X,500}$ as a function of halo mass obtained by Anderson et al. (2015) is very similar to that obtained by Wang et al. (2014).

3. MODELS OF HALO GAS

In this section, we describe our methods to model the density and temperature of gas in halos. We use the electron number density, n_e , to represent the density of the gas. We also assume that the gas temperature is the same as the electron temperature, T_e . We examine a number of different cases with different assumptions of the gas density and temperature.

3.1. Single phase models

As our fiducial assumption for the gas density, we use the following profile:

$$n_e(M_{200}, r) = n_0(M_{200}) [1 + (r/r_c)^2]^{-3\beta/2}, \quad (10)$$

where $r_c = R_{200}/c$, with c being the concentration of the halo, and $\beta = 0.86$. The amplitude of the profile, n_0 , is assumed to depend on M_{200} , and we use the c - M_{200} relation given by Bullock et al. (2001) to compute r_c . This profile is adopted from Plagge et al. (2010) and is the same as that used in Lim et al. (2018). The first set of models we consider assume that all the halo gas is in a single phase with a given temperature profile, T_h . This set of models are denoted by $M1$.

The simplest assumption in modeling the hot gas temperature in galaxy groups/clusters is that the gas is at the virial temperature,

$$T_{vir} = \mu \frac{GM_{vir}m_p}{2k_B r_{vir}}, \quad (11)$$

where M_{vir} and r_{vir} are the virial mass and radius of the halo, respectively, m_p is the proton mass, μ is the mean molecular weight, G is the gravitational constant. In our analysis we take $M_{vir} = M_{200}$ and $r_{vir} = R_{200}$.

We therefore consider a model, $M1 - T_{vir}$, where the hot gas temperature is assumed to be uniform within halos and is equal to T_{vir} , and the gas density is given by equation (10) with $n_0(M_{200})$ constrained by the observational data.

More generally, we follow [Loken et al. \(2002\)](#) and consider models in which the gas temperature profile is given by

$$T(M_{200}, r) = T_0(M_{200}) [1 + 1.5(r/R_{200})]^{-1.6}, \quad (12)$$

where $T_0(M_{200})$ is the amplitude of the profile which is to be constrained by observational data.

In general, the two amplitudes, n_0 and T_0 , can both depend on halo mass, M_{200} , and the dependence may not be deterministic. During the analyzing, we use n_0 in unit of m^{-3} and T_0 in unit of K. To allow variance in the relations, we use the following model for $n_0(M_{200})$:

$$\log_{10}(n_0) = \mathcal{N}(\mu_n, \sigma_n), \quad (13)$$

where $\mathcal{N}(\mu, \sigma)$ is a normal distribution with mean μ and variance σ . We find that the observational data can be described by the following simple assumptions:

$$\mu_n = \mu_{n0} + \alpha_n \log_{10} \left[\frac{M_{200}}{3 \times 10^{14} M_\odot} \right], \quad (14)$$

and

$$\sigma_n = \sigma_{n0} + \beta_n \log_{10} \left[\frac{M_{200}}{3 \times 10^{14} M_\odot} \right], \quad (15)$$

where μ_{n0} , α_n , σ_{n0} and β_n are model parameters to be determined by the observational data. Similarly, for the gas temperature, we assume

$$\log_{10}(T_0) = \mathcal{N}(\mu_T, \sigma_T), \quad (16)$$

with

$$\mu_T = \mu_{T0} + \alpha_T \log_{10} \left[\frac{M_{200}}{3 \times 10^{14} M_\odot} \right], \quad (17)$$

and

$$\sigma_T = \sigma_{T0} + \beta_T \log_{10} \left[\frac{M_{200}}{3 \times 10^{14} M_\odot} \right]. \quad (18)$$

The model parameters, μ_{T0} , α_T , σ_{T0} and β_T are again to be constrained by observational data. We assume

that the variances in the density and temperature are independent, so that they can affect the predicted mean only for L_X , but the predicted dispersion for all three observational quantities may be affected. Based on these assumptions on gas density and temperature, we consider models in which variances are allowed in n_0 or T_0 , or in both, as listed in Table 1.

3.2. Two-phase models

Because of processes like radiative cooling, feedback, thermodynamic and hydrodynamic instabilities, halo gas is expected to be a multi-phase medium consisting of gas components at different temperatures ([Mo et al. 2010](#), e.g. chapter 8.). Unfortunately, the detail of such multi-phase media is poorly understood. Here we consider a simple case in which the halo gas is a two-phase medium, with a hot component at temperature T_h and a warm component with temperature T_w , both assumed to be fully ionized. These two components are assumed to be in pressure equilibrium, so that at any given location

$$n_h T_h = n_w T_w, \quad (19)$$

where n_h and n_w are the local densities of the hot and warm components, respectively. We model the mass fraction in the hot component as

$$f_h \equiv \frac{M_h}{M_h + M_w} = f_{h0} \left(\frac{M_{200}}{M_0} \right)^{\alpha_f}, \quad (20)$$

where M_h and M_w are the total masses in the two components, respectively. The volume filling factors of the two components, ϕ_h and ϕ_w , are defined as

$$\phi_h \equiv \frac{V_h}{V_h + V_w} = 1 - \phi_w, \quad (21)$$

so that

$$\frac{M_h}{M_w} = \frac{n_h \phi_h}{n_w \phi_w} = \frac{f_h}{1 - f_h}. \quad (22)$$

It can then be shown that

$$\phi_h = \frac{T_h f_h}{T_h \cdot f_h + T_w (1 - f_h)}. \quad (23)$$

Finally, the total gas density and pressure can be written as

$$n_e = n_h \phi_h + n_w \phi_w = n_h \left(\phi_h + \frac{T_h}{T_w} \phi_w \right), \quad (24)$$

and

$$P_e = \frac{n_e T_h}{\phi_h + \phi_w T_h / T_w}. \quad (25)$$

As one can see, once models are adopted for n_e , T_h , T_w and f_h , one can make model predictions for the kSZE

Table 1. Models of halo gas.

Model	Gas phase	Variance in T_0	Variance in n_0
M1- T_{vir}	1-phase	No; $T = T_{vir}$	No
M1-no scatter	1-phase	No	No
M1- T_0	1-phase	Yes	No
M1- n_0	1-phase	No	Yes
M1- T_0, n_0	1-phase	Yes	Yes
M2- T_{vir}	2-phase	No; $T = T_{vir}$	Yes
M2-no scatter	2-phase	No	No
M2- T_0	2-phase	Yes	No
M2'- T_0	2-phase	Yes	No; a flatter n_e profile
M2- n_0	2-phase	No	Yes
M2- T_0, n_0	2-phase	Yes	Yes

through n_e and for the tSZE through P_e . For the X-ray luminosity, we assume that the warm component contributes little, so that it can be obtained through n_h and T_h in the volume occupied by the hot component specified by ϕ_h .

For all the two-phase models, listed as M2 in Table 1, we assume that $T_w = 10^5$ K at the halo center and follows the same profile as T_h . Since the volume occupied by the warm phase is in general much smaller than that occupied by the hot phase, the exact value assumed for T_w is not important, provided that it is much smaller than T_h and sufficiently high to ensure the ionization fraction is close to one. We also assume that f_h is described by equation (20), n_e by equation (10), and T_h is either equal to T_{vir} (Model M2- T_{vir}) or described by equation (12) with T_0 being the temperature at halo center. Similar to the single phase models, variances in n_0 and T_0 are included in some of the two-phase models, as described in Table 1. We adopt the β -model of equation (10) for the n_e profile, with the concentration parameter c describing the core radius. A higher c leads to more concentrated distribution of the gas. As mentioned earlier, we use the model of Bullock et al. (2001) for c as a function of halo mass. To examine the impact of the assumed gas profile on our results, we also consider a new model, M2'- T_0 , which is the same as M2- T_0 except that the concentration parameter is reduced by a factor of two.

4. ANALYSIS AND RESULTS

To constrain a model with observational data, we generate a set of n_e and T_h for a given set of model parameters. We then compute the corresponding \tilde{K}_{200} , P_{200} and $L_{X,500}$, and compare them with the observational data. For X-ray, we integrate the X-ray flux within R_{500} to compare with observation. The comparison between model predictions and observational data is through the likelihood function,

Table 2. Prior ranges of the model parameters and the relevant equations are listed. Posteriors for the M2- T_0, n_0 model are listed as an example. Details of the models can be found in section 3.

Name	Prior	Posterior	Relevant equation
α_T	[0.5,1.8]	0.79±0.07	Equation 17
μ_{T0}	[5.5,8.5]	7.89±0.07	Equation 17
σ_{T0}	[0,0.2]	0.08±0.06	Equation 18
β_T	[-1,0]	-0.20±0.16	Equation 18
α_N	[-0.4,0.4]	0.17±0.07	Equation 17
μ_{n0}	[2.5,4.5]	3.36±0.05	Equation 14
σ_{n0}	[0,0.2]	0.06±0.04	Equation 15
β_n	[-1,0]	-0.31±0.19	Equation 15
α_f	[0,0.6]	0.20±0.06	Equation 20
f_{h0}	[0.3,0.9]	0.32±0.07	Equation 20

$$\mathcal{L} = \prod_i \frac{1}{\sqrt{2\sigma_i}} \exp \left[-\frac{(\mathcal{M}_i(\Theta) - \mathcal{D}_i)^2}{2\sigma_i^2} \right], \quad (26)$$

where $\mathcal{M}_i(\Theta)$ is the prediction of the model specified by the parameter set Θ for the i th data point, \mathcal{D}_i is the corresponding observational data and σ_i is its error. The posterior distribution of model parameters is sampled with the PyMultinest, a Python module of the MultiNest sampling engine for both parameter estimation and model selection (Buchner et al. 2014). We assume a flat prior for each parameter, with its range chosen sufficiently broad (see Table 2). For reference, the posterior model parameters obtained from M2- T_0, n_0 are also shown in Table 2.

To examine how different models can accommodate the observational data, we compute the Bayesian evidence,

$$\mathcal{E}(\mathcal{M}) = \int \mathcal{P}(\mathcal{D}|\mathcal{M}, \Theta) \mathcal{P}(\Theta|\mathcal{M}) d\Theta, \quad (27)$$

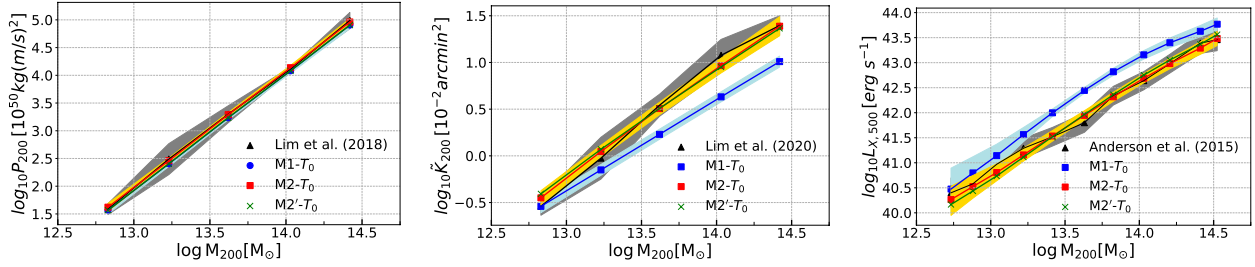


Figure 1. Observational data used to constrain models. The black points and shadow regions are the mean and dispersion, respectively. The left, middle and right panels are, respectively, the tSZE, kSZE and L_X , all plotted versus halo mass, M_{200} . For comparison, we plot the posterior predictions of three constrained models. Blue lines are for the single phase model, M1- T_0 , red lines for the two-phase model, M2- T_0 and green line for M2'- T_0 . The shadow regions around the blue and red lines are the 90 percentile ranges derived from the posterior distributions.

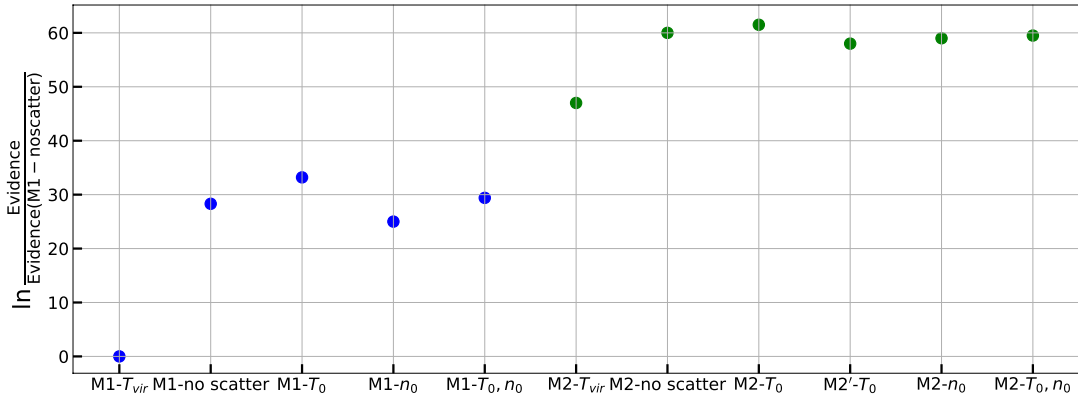


Figure 2. Bayesian evidences of different models with respect to M1- T_{vir} . Blue points represent the set of single phase models (M1), while green points are for the set of two-phase models (M2).

where $\mathcal{P}(\mathcal{D}|\mathcal{M}, \Theta)$ is the probability of the data given model \mathcal{M} with a given set of model parameters, Θ , and $\mathcal{P}(\Theta|\mathcal{M})$ is the prior distribution of model parameters. So defined, the Bayesian evidence is the probability of the observational data in a model family \mathcal{M} , and thus can be used to compare different model families in their abilities to accommodate the observational data. Figure 2 shows the logarithms (to natural base) of the Bayesian evidence ratio, $\ln(\mathcal{E}(\mathcal{M})/\mathcal{E}(\mathcal{M}_0))$, of a given model \mathcal{M} relative to the reference model, \mathcal{M}_0 , which is chosen to be M1- T_{vir} . As one can see, all the two-phase models give a similar evidence ratio, about 60 in logarithmic scales, while all the single-phase models have a ratio about 30. Typically, a Bayesian evidence ratio of more than 20 in logarithmic scale indicates a significant preference between the two models in comparison. It is thus clear that the combination of the tSZE, kSZE and L_X data has a significant preference to the two-phase hypothesis (M2), while a single phase model with gas at the virial temperature is the least favored.

To see more clearly how the models fit observational data, we use the posterior distribution of each individual model to predict the observations. As exam-

ples, the predictions of M1- T_0 and M2- T_0 are shown in Figure 1. Clearly, M1- T_0 cannot accommodate the three sets of observational data simultaneously: it significantly under-predicts kSZE but over-predicts L_X . In contrast, M2- T_0 matches well all the three observations. We find that the results of these two models represent well those of the two model sets, M1 and M2, indicating that the key to match the observational data is the assumption of a two-phase medium, while other details, such as the inclusion of scatter in model parameters, only play a minor role. We find that model M2- T_{vir} matches the observational data only slightly worse than the other M2 models, suggesting that the average hot gas temperature needed to fit the data is not very different from T_{vir} . Model M2'- T_0 has a Bayesian evidence similar to M2- T_0 , and their posterior predictions for the three sets of observations are also very similar, indicating that these observations do not provide a strong constraint on the gas density profile. However, as we will show below, the change of gas density profile can affect the model inferences significantly.

We can use the posterior model distributions to make predictions for the gas mass and temperature as func-

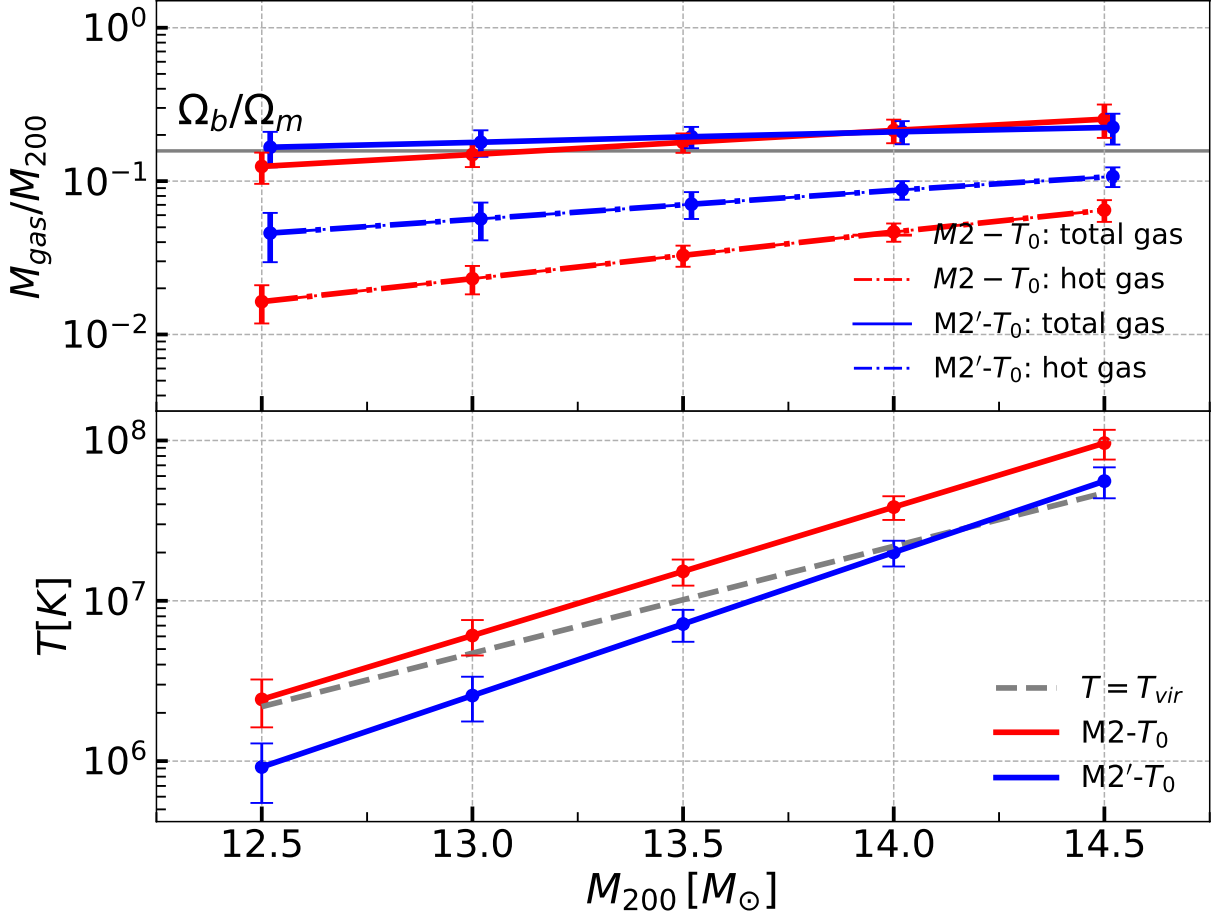


Figure 3. Top panel: the gas mass fractions predicted by $M2-T_0$ (red) and $M2'-T_0$ (blue). Solid lines show the total gas mass fraction, while dot-dashed lines are for the hot gas mass fraction. Error bars are the 90 percentile range of the predictions based on the posterior distributions. Gray shadow region shows the cosmic baryon fraction, $\Omega_b/\Omega_m = 0.1574 \pm 0.002$, as given by Planck cosmology (Planck Collaboration et al. 2016a). The results of $M2'-T_0$ are slightly shifted horizontally for clarity. Bottom panel: hot gas temperature as a function of M_{200} predicted by $M2-T_0$ (red) and $M2'-T_0$ (blue). Error bars represents the 90 percentiles of T_h derived from the posterior distribution. Gray dashed line is $T_{\text{vir}}(M_{200})$.

tions of halo mass. Here again we use $M2-T_0$ and $M2'-T_0$ as demonstrations. We estimate the baryon mass in halos of a given mass by integrating the corresponding gas density profile within R_{200} , assuming a fully ionized primordial gas with a hydrogen mass fraction of $f_H = 0.76$. In the top panel of Figure 3 we show the total and hot gas masses, both normalized by halo mass, versus the halo mass. Red and blue lines are for $M2-T_0$ and $M2'-T_0$, respectively, while solid and dot-dashed lines are for the total and hot gas, respectively. For all cases, the error bars represent the 90 percentile of the posterior predictions. For comparison we also show the universal baryon fraction from Planck Collaboration et al. (2016a) as the horizontal gray band⁴.

⁴ The variance of universal baryon fraction is small here, so in the plot, the shadow region of baryon fraction just looks like a line.

The posterior predictions of the central temperature of the hot gas component, $T_0(M_{200})$, by $M2-T_0$ and $M2'-T_0$ are shown in the bottom panel of Figure 3, together with the virial temperature, $T_{\text{vir}}(M_{200})$, given by equation (11).

The total gas mass fraction predicted is comparable to the universal baryon fraction, a result of the constraints mainly from the kSZE observation. The hot gas mass fraction predicted by $M2'-T_0$ is higher than that by $M2-T_0$, because X-ray emission is less efficient for the more extended gaseous halos in $M2'-T_0$. In both cases, the hot gas mass fraction increases with M_{200} with a logarithmic slope of about 0.2, but is significantly lower than the universal fraction. For $M2-T_0$, the ratio between the hot gas fraction and the universal fraction increases from ~ 0.15 to ~ 0.4 as halo mass changes from $10^{12.5} M_{\odot}$ to $10^{14.5} M_{\odot}$; for $M2'-T_0$, the increases is from ~ 0.4 to ~ 0.6 . This suggests that a large fraction of the halo

gas is in an ionized phase with temperature much lower than the virial temperature.

Because of the constraints from the tSZE, the hot gas temperature is required to be lower in $M2'-T_0$ than in $M2-T_0$ by a factor about two. For both of these models, the central hot gas temperature, T_0 , is comparable to the halo virial temperature within a factor of two. The predicted T_0-M_{200} relations have a logarithmic slope of about 0.8, slightly steeper than that of the $T_{vir}-M_{200}$ relation.

The differences in the posterior predictions of the hot gas fraction and temperature between $M2-T_0$ and $M2'-T_0$ suggest that there is significant degeneracy between the mass of hot gas halos and their profiles. Thus, without additional information about the profile, it is difficult to obtain stringent constraints on the hot halo gas. The β -profile of equation (10) is motivated by observations of massive clusters (e.g. McDonald et al. 2017), and is roughly consistent with the hot gas profiles of clusters in gas simulations (Lim et al. 2020 to be submitted). For halos of lower masses, the hot gas profile is not well known from observation. In numerical simulations, the gas profiles of these lower-mass halos can be affected significantly by feedback. Using data from EAGLE (Schaye et al. 2015) and Illustris TNG (Nelson et al. 2019; Marinacci et al. 2018; Naiman et al. 2018; Nelson et al. 2018; Pillepich et al. 2018; Springel et al. 2018), Lim et al. (2020, to be submitted) found that the β -model is a rough approximation to the halo gas in low-mass halos, provided that the core radius r_c is increased by a factor of two. Thus, the results of models $M2-T_0$ and $M2'-T_0$ may represent the range expected from the uncertainties in the hot gas profile. However, if the core radius r_c in equation (10) were comparable to the virial radius for low-mass halos, the inferred mass in the hot component would approach the universal fraction, leaving no room for the presence of the warm component. In this case, the gas temperature would be about 10 times lower than the corresponding virial temperature, as shown in Lim et al. (2020).

5. SUMMARY AND DISCUSSION

In this work, we combine observational data of kSZE, tSZE and L_X to constrain the density and temperature of diffuse gas in halos. We use a number of generic models and a Bayesian scheme to explore the constraints provided by the observational data. Our main results can be summarized as follows.

- Single phase models, in which all the halo gas is assumed to have similar temperature, cannot accommodate the observational data, suggesting that halo gas is not completely thermalized to a

single phase. The tension may be alleviated if the gas density profile is much shallower than that seen in numerical simulations.

- Simple two-phase models, which assume a hot gas component and an ionized warm component in pressure equilibrium, can match well with the observational data without depending on model details.
- The predicted total (hot plus warm) gas mass fraction in individual halos is comparable to the universal baryon fraction, suggesting that most halos can retain most of the baryons in their possession.
- The hot gas component in a halo has a temperature that is comparable to the virial temperature of the halo.
- The fraction of the hot component is found to increase from (15 – 40)% for $10^{12.5}M_\odot$ halos to (40 – 60)% for $10^{14.5}M_\odot$ halos, where the lower and upper bounds cover uncertainties in the assumed density profiles.

Our results have important implications for galaxy formation and evolution. Observations have shown that star formation in the universe is inefficient and that only a small fraction of the baryons is locked in stars (e.g. Li & White 2009). To prevent baryons from forming stars too quickly, feedback processes are invoked either to heat the star forming gas or to eject it from galaxies. All numerical simulations of galaxy formation in the current paradigm need to incorporate some feedback processes to reproduce the stellar component observed in the universe. Most of the simulations seem to show the existence of hot gaseous halos with an average gas temperature comparable to the halo virial temperature and with mass significantly smaller than that implied by the universal baryon fraction (e.g. Lim et al. 2020 to be submitted). These are consistent with our results for the hot gas component. However, in these simulations, a significant fraction of the baryons is ejected from halos by feedback effects, so that the warm phase implied by our results is insignificant. This indicates that the current cosmological simulations may not be able to resolve multi-phase media or may have missed a significant non-thermalized gas component in gaseous halos. Indeed, using high-resolution zoom-in simulations of clusters of galaxies, Nelson et al. (2014) found that a significant fraction of the gas pressure is non-thermal pressure produced by the bulk motion of cooler gas. This is consistent with the results that a substantial fraction of the gas in clusters is in a phase with temperature much lower

than the virial temperature. For low-mass halos, the presence of a gas component at temperature lower than the virial temperature has been probed by QSO absorption line systems such as MgII and OVI (e.g. [Werk et al. 2014](#); [Zhu et al. 2014](#); [Lan & Mo 2018](#)). Unfortunately, the total amount of the gas implied by these systems are still uncertain (e.g. [Tumlinson et al. 2017](#)).

Clearly, with data from large, high-resolution CMB surveys, such as CMB-S4, and all sky X-ray surveys, such as eROSITA, we hope to obtain much better con-

straints on the gaseous halos over a large mass range, so as to provide important insight about the processes by which gaseous halos and galaxies form and evolve.

ACKNOWLEDGMENTS

This work is supported by the National Key R&D Program of China (grant No. 2018YFA0404502, 2018YFA0404503), and the National Science Foundation of China (grant Nos. 11821303, 11973030, 11673015, 11733004, 11761131004, 11761141012).

REFERENCES

- Anderson, M. E., Gaspari, M., White, S. D. M., Wang, W., & Dai, X. 2015, *MNRAS*, 449, 3806, doi: [10.1093/mnras/stv437](#)
- Arnaud, M., & Evrard, A. E. 1999, *MNRAS*, 305, 631, doi: [10.1046/j.1365-8711.1999.02442.x](#)
- Arnaud, M., Pratt, G. W., Piffaretti, R., et al. 2010, *A&A*, 517, A92, doi: [10.1051/0004-6361/200913416](#)
- Babul, A., Balogh, M. L., Lewis, G. F., & Poole, G. B. 2002, *MNRAS*, 330, 329, doi: [10.1046/j.1365-8711.2002.05044.x](#)
- Buchner, J., Georgakakis, A., Nandra, K., et al. 2014, *A&A*, 564, A125, doi: [10.1051/0004-6361/201322971](#)
- Bullock, J. S., Kolatt, T. S., Sigad, Y., et al. 2001, *MNRAS*, 321, 559, doi: [10.1046/j.1365-8711.2001.04068.x](#)
- Cavaliere, A., Menci, N., & Tozzi, P. 1998, *ApJ*, 501, 493, doi: [10.1086/305839](#)
- Helsdon, S. F., & Ponman, T. J. 2000, *MNRAS*, 319, 933, doi: [10.1046/j.1365-8711.2000.03916.x](#)
- Kravtsov, A. V., & Yepes, G. 2000, *MNRAS*, 318, 227, doi: [10.1046/j.1365-8711.2000.03771.x](#)
- Lan, T.-W., & Mo, H. 2018, *ApJ*, 866, 36, doi: [10.3847/1538-4357/aadc08](#)
- Li, C., & White, S. D. M. 2009, *MNRAS*, 398, 2177, doi: [10.1111/j.1365-2966.2009.15268.x](#)
- Lim, S. H., Mo, H. J., Li, R., et al. 2018, *ApJ*, 854, 181, doi: [10.3847/1538-4357/aaa21](#)
- Lim, S. H., Mo, H. J., Wang, H., & Yang, X. 2020, *ApJ*, 889, 48, doi: [10.3847/1538-4357/ab63df](#)
- Loken, C., Norman, M. L., Nelson, E., et al. 2002, *ApJ*, 579, 571, doi: [10.1086/342825](#)
- Marinacci, F., Vogelsberger, M., Pakmor, R., et al. 2018, *MNRAS*, 480, 5113, doi: [10.1093/mnras/sty2206](#)
- McCarthy, I. G., Schaye, J., Bower, R. G., et al. 2011, *MNRAS*, 412, 1965, doi: [10.1111/j.1365-2966.2010.18033.x](#)
- McDonald, M., Allen, S. W., Bayliss, M., et al. 2017, *ApJ*, 843, 28, doi: [10.3847/1538-4357/aa7740](#)
- Mo, H., van den Bosch, F. C., & White, S. 2010, *Galaxy Formation and Evolution*
- Naiman, J. P., Pillepich, A., Springel, V., et al. 2018, *MNRAS*, 477, 1206, doi: [10.1093/mnras/sty618](#)
- Nelson, D., Pillepich, A., Springel, V., et al. 2018, *MNRAS*, 475, 624, doi: [10.1093/mnras/stx3040](#)
- Nelson, D., Springel, V., Pillepich, A., et al. 2019, *Computational Astrophysics and Cosmology*, 6, 2, doi: [10.1186/s40668-019-0028-x](#)
- Nelson, K., Lau, E. T., & Nagai, D. 2014, *ApJ*, 792, 25, doi: [10.1088/0004-637X/792/1/25](#)
- Pillepich, A., Nelson, D., Hernquist, L., et al. 2018, *MNRAS*, 475, 648, doi: [10.1093/mnras/stx3112](#)
- Plagge, T., Benson, B. A., Ade, P. A. R., et al. 2010, *ApJ*, 716, 1118, doi: [10.1088/0004-637X/716/2/1118](#)
- Planck Collaboration, Ade, P. A. R., Aghanim, N., et al. 2013, *A&A*, 557, A52, doi: [10.1051/0004-6361/201220941](#)
- . 2014, *A&A*, 571, A21, doi: [10.1051/0004-6361/201321522](#)
- . 2016a, *A&A*, 594, A13, doi: [10.1051/0004-6361/201525830](#)
- Planck Collaboration, Aghanim, N., Arnaud, M., et al. 2016b, *A&A*, 594, A11, doi: [10.1051/0004-6361/201526926](#)
- Remazeilles, M., Delabrouille, J., & Cardoso, J.-F. 2011, *MNRAS*, 410, 2481, doi: [10.1111/j.1365-2966.2010.17624.x](#)
- Rephaeli, Y., Sadeh, S., & Shimon, M. 2005, in *Background Microwave Radiation and Intracluster Cosmology*, ed. F. Melchiorri & Y. Rephaeli, 57
- Schaye, J., Crain, R. A., Bower, R. G., et al. 2015, *MNRAS*, 446, 521, doi: [10.1093/mnras/stu2058](#)
- Springel, V., Pakmor, R., Pillepich, A., et al. 2018, *MNRAS*, 475, 676, doi: [10.1093/mnras/stx3304](#)

- Sunyaev, R. A., & Zeldovich, Y. B. 1970, *Ap&SS*, 7, 3,
doi: [10.1007/BF00653471](https://doi.org/10.1007/BF00653471)
- . 1972, *Comments on Astrophysics and Space Physics*, 4,
173
- Tumlinson, J., Peeples, M. S., & Werk, J. K. 2017,
ARA&A, 55, 389,
doi: [10.1146/annurev-astro-091916-055240](https://doi.org/10.1146/annurev-astro-091916-055240)
- Wang, H., Mo, H. J., Yang, X., & van den Bosch, F. C.
2012, *MNRAS*, 420, 1809,
doi: [10.1111/j.1365-2966.2011.20174.x](https://doi.org/10.1111/j.1365-2966.2011.20174.x)
- Wang, L., Yang, X., Shen, S., et al. 2014, *MNRAS*, 439,
611, doi: [10.1093/mnras/stt2481](https://doi.org/10.1093/mnras/stt2481)
- Werk, J. K., Prochaska, J. X., Tumlinson, J., et al. 2014,
ApJ, 792, 8, doi: [10.1088/0004-637X/792/1/8](https://doi.org/10.1088/0004-637X/792/1/8)
- Zhu, G., Ménard, B., Bizyaev, D., et al. 2014, *MNRAS*,
439, 3139, doi: [10.1093/mnras/stu186](https://doi.org/10.1093/mnras/stu186)